Phase transition influenced Photocatalytic dye degradation capability of pure and Eu-doped $CoMoO_4$ polymorphic nanostructures

R. Rahul[a], Govarthini Seerangan Selvam[b], S. Moorthy Babu[c], Alagar Muthukaruppan [d], G. Bhoopathi [a*], S Nanthakumar[e], Thangaraju Dheivasigamani [b*].

[a] *Department of Physics, PSG College of Arts and Science, Coimbatore-641 014, Tamil Nadu, India.*

[b]*Nano-crystal Design and Application Lab (n-DAL), Department of Physics, PSG Institute of Technology and Applied Research, Coimbatore-641 062, Tamil Nadu, India.*

[c] *Crystal Growth Centre, Anna University, Chennai, 600 025, Tamil Nadu, India.*

[d] *Polymer Engineering Lab (PEL), Department of Chemistry, PSG Institute of Technology and Applied Research, Coimbatore-641 062, Tamil Nadu, India.*

[e] *Department of Mechanical Engineering, PSG Institute of Technology and Applied Research, Coimbatore-641 062, Tamil Nadu, India.*

* Corresponding author

E-mail address: dthangaraju@gmail.com (Thangaraju Dheivasigamani)

Abstract

The efficient degradation of organic dyes via photocatalysis presents a critical environmental challenge, necessitating advancements in catalyst design and performance. This study investigates the potential of pure and Eu doped $CoMoO_4$ polymorphic nanostructures in addressing this challenge. Our primary focus is on enhancing the efficiency and stability of photocatalysts under diverse condition by performing sol-gel synthesis. Characterization techniques such as X-ray diffraction (XRD), scanning electron microscopy (SEM), ultraviolet-visible (UV-visible) analysis and Raman analysis was employed to elucidate structural and morphological changes. Our results highlight the significant enhancement in photocatalytic activity achieved through phase transitions induced by Eu doping. This enhancement is attributed to the creation defect sites and the establishment of improved charge transfer pathways within the $CoMoO_4$ nanostructures. By shedding light on the role of phase transition in photocatalysis, this study contributes valuable insights for the design of efficient and durable photocatalysts for environmental remediation application.

.

Keywords: $CoMoO_4$, nano-particles, monoclinic, photocatalysis, methylene blue.

1. Introduction

Methylene blue (MB) is a dye commonly used in various industries, including textile manufacturing, laboratory procedures, and medical diagnostics. However, despite its widespread use, concerns have arisen regarding its potential negative impact on human health and the environment. Methylene blue can be toxic if ingested or absorbed through the skin in large quantities. It may cause symptoms such as nausea, vomiting, abdominal pain, dizziness, and methemoglobinemia, a condition in which the blood capacity to carry oxygen is impaired[1]. Some individuals may experience allergic reactions to methylene blue, ranging from skin irritation to more severe hypersensitivity reactions. The disposal of wastewater contaminated with methylene blue can cause environmental pollution, affect aquatic ecosystems, and potentially contaminate drinking water sources[2]. Efforts are underway to develop more efficient wastewater treatment processes capable of removing methylene blue and other dyes from industrial effluents before discharge into the environment. Techniques such as adsorption, oxidation, and biological degradation have been used for dye removal[3]. Recent advances in dye degradation and decolorization have focused on developing efficient, cost-effective, and environment-friendly methods to address water pollution challenges. Several innovative approaches that leverage diverse technologies and materials have emerged. Recently developed methods have been used for the degradation and decolorization of dyes. Advanced oxidation processes (AOPs), such as photocatalysis, ozonation, and electrochemical oxidation have gained attention for their ability to effectively degrade dyes [4–6]. Photocatalytic degradation using semiconductor photocatalysts such as titanium dioxide (TiO_2) or zinc oxide (ZnO) harnesses light energy to generate reactive oxygen species that degrade dyes into non-toxic byproducts [7]. Biological methods and degradation using enzymes, microorganisms, and algae offer a sustainable approach to dye removal. Enzymes, such as laccase, peroxidase, and azoreductase, have been utilized for their ability to degrade various

dye molecules. Bioremediation techniques that employ bacterial consortiums or genetically engineered microorganisms have shown promise in breaking down complex dye structures [8]. Nanostructured materials, including nanoparticles, nanocomposites, and nanotubes, exhibit enhanced adsorption and catalytic properties for dye degradation [9]. Metal-organic frameworks (MOFs) and carbon-based nanomaterials such as graphene and carbon nanotubes have been explored for their high surface area and reactivity in dye degradation [7]. Hybrid approaches that combine multiple techniques, such as photocatalysis with adsorption or biological treatment with AOPs, have been proposed to synergistically improve the dye degradation efficiency [10]. Integrated systems incorporating physical, chemical, and biological processes offer comprehensive solutions for complex dye wastewater treatment[11]. Green chemistry principles, including the use of renewable resources, non-toxic reagents, and benign reaction conditions, are being integrated into dye degradation methods to minimize environmental impacts [12] . Sustainable solvents, microwave-assisted processes, and catalytic reactions have been explored to optimize energy efficiency and reduce chemical waste generation [9,13]. In general, no one size fits all solutions, and the choice of method depends on a careful evaluation of factors, such as treatment efficiency, cost-effectiveness, environmental impact, and scalability. In many cases, a combination of methods or AOP may be the most effective strategy to achieve comprehensive dye effluent treatment and water pollution control. Nanoparticles have emerged as versatile materials for dye degradation in wastewater treatment, owing to their high surface area, reactivity, and tunable properties. Several types of nanoparticles have been investigated for this purpose, each offering unique advantages and drawbacks. TiO_2 nanoparticles have been widely studied for photocatalytic degradation of dyes because of their stability, low cost, and high photocatalytic activity under UV light[11,14]. However, their efficiency is limited to UV light absorption, and they exhibit rapid electron-hole recombination, leading to reduced overall performance [12]. ZnO

nanoparticles possess excellent photocatalytic activity and can absorb both ultraviolet (UV) and visible light, making them suitable for dye degradation under solar irradiation[15,16]. However, their tendency to aggregate and photo corrosion limits their long-term stability and efficiency [17]. Iron-based nanoparticles, such as Fe_3O_4 and Fe_2O_3, are effective for the degradation of dyes through Fenton-like reactions, generating highly reactive hydroxyl radicals. Although they offer high catalytic activity, issues such as aggregation, limited reusability, and the need for additional activation methods hinder their practical applications[18]. $CoMoO_4$ nanoparticles have recently gained attention for dye degradation owing to their unique properties and advantages over other nanoparticles. They exhibit enhanced photocatalytic activity under both UV and visible light irradiation owing to their broad absorption range and efficient charge-separation capabilities [19]. Furthermore, $CoMoO_4$ nanoparticles demonstrated high stability, recyclability, and multifunctionality, making them suitable for continuous and efficient dye wastewater treatment. Their facile synthesis methods and scalability contribute to their appeal for industrial applications [20]. These properties suggest that $CoMoO_4$ is a promising candidate for sustainable and efficient dye-wastewater treatment.

Here, we investigate the $CoMoO_4$ nanoparticle synthesis process using the modified solution combustion method[21–23]. Inspired by these reports, here in this work we have synthesized pure $CoMoO_4$ and Europium-Doped nanoparticles in the (2.5,5,7.5and 10 wt. %) and they were characterized using various techniques, such as X-ray diffraction (XRD), scanning electron microscopy (SEM), ultraviolet-visible analysis (UV-vis), and Raman spectroscopy, to assess their crystallinity, morphology, and chemical composition. The proposed modified solution combustion method is simple and cost-effective with a controlled morphology for synthesis. This method provides a facile and versatile approach for synthesizing $CoMoO_4$ nanoparticles with tailored properties for photocatalytic applications.

2. Materials and methods

2.1 Materials

Ammonium heptamolybdate tetrahydrate ($(NH_4)_6Mo_7O_{24}\cdot 4H_2O$, Merck), Cobalt (II) nitrate hexahydrate (Co $(NO_3)_2\cdot 6H_2O$), Merck, ethylene glycol ($C_2H_6O_2$, Hi Media), europium nitrate hexahydrate (Eu $(NO_3)_3\cdot 6H_2O$), and citric acid monohydrate ($C_6H_8O_7\cdot H2O$, Sisco), were utilized without being purified further. Methylene blue was used as a model pollutant in the study of photocatalytic activity.

2.2 Preparation of photocatalysts

$CoMoO_4$ composites were synthesized from stoichiometric amounts of Co $(NO)_2.6H_2O$ having a molecular weight of 291.04g/ mol. and $(NH_4)_6Mo_7O_{24}.4H_2O$ having a molecular weight of 123686g/mol, which are used as the Cobalt and Molybdate sources, respectively. The synthesis was done through a modified solution combustion synthesis procedure [24,25]. About 1.527g of $Co(NO_3)_2.6H_2O$ was dissolved in 20 ml deionized water in a 1:7 ratio, and 0.927g of $(NH_4)_6Mo_7O_{24}.4H_2O$ was dissolved in 20 ml deionized water separately for about 20 minutes. The two solutions were mixed while the temperature was kept at 70°C, and 1.260 g of citric acid was added with effective agitation. The temperature of the solution was increased to and kept at 80° C, and then 20 drops of ethylene glycol were added with thorough mixing by steady stirring through which the pH was maintained at 10, after 5 hrs. the gel obtained was transferred into a silica crucible and then gradually annealed at 550°C and 950°C to obtain different crystal phases. The temperatures at 550°C and 950°C subsequently leads to the formation of α- $CoMoO_4$ and β- $CoMoO_4$ polymorphs [26,27]. A similar procedure was adopted to incorporate dopant europium nitrate hexahydrate [Eu $(NO_3)_3.6H_2O$,] having a

molecular weight of 337.98g/mol, with varying concentrations of 2.5%, 5%, 7.5%, 10%. The samples were preserved for further characterization.

2.3. Characterization Techniques

To determine phase formation, crystallite size, and shape, $CoMoO_4$ was characterized using a variety of current analytical methods. The crystalline structure of $CoMoO_4$ was investigated using a Rigaku Ultima X-ray diffractometer with Cu-K radiation (λ =1.5418). Raman spectrum analysis was captured using a laser Raman Microscope (Raman-11,500 mm spectrometer Nano photon Corporation Japan). Scanning electron microscopy (SEM), images were produced using the LEO-1455VP instrument. The optical characteristics and band gap energy (Eg) were studied using a Jasco V-650 Ultraviolet spectrometer. The occurrence of photocatalytic processes was studied using a Shimadzu-1380 UV/Vis-NIR spectrophotometer and the change in methylene blue absorbance intensity.

2.4. Dye Degradation mechanism

The schematic illustration of possible photocatalytic mechanism for the photodegradation of MB dye is shown in Figure 1.The plausible degradation mechanism of MB dye in the presence of optimized Pure $CoMoO_4$ catalyst under visible light irradiation is as follows [28]. As the doping of Eu forms the impurity levels above the valence band maxima in the $CoMoO_4$ band structure thereby reduces the band gap of $CoMoO_4$. The enhanced optical response of the Eu doped $CoMoO_4$ powder is due to the rapid electron transfer from these impurity levels to the conduction band of $CoMoO_4$. When photons with energy higher than $CoMoO_4$ band gap are adsorbed on the surface of Eu -doped $CoMoO_4$ nanoparticles. Excitation of electron from valence band to conduction band creates electron (e^-) in the conduction band and hole (h^+) in the valence band (Eq. 1). The positive hole (h^+) reacts with the hydroxide ions or water molecules adsorbed on the surface of $CoMoO_4$ and can produce free hydroxyl radicals

(OH•) (Eqs. 2 and 3). Next, the conduction band electrons (e^- CB) can react with the oxygen to produce O_2 •− super oxide radical anions, which may oxidize organic pollutants into small molecules (Eq. 4). Further, a part of O_2 •− can react with H^+ to produce H_2O_2, which is further reduces to OH• radicals after excitation from electrons (Eqs. 5, 6 and 7)[14,29,30].Finally, free radicals (OH•) and (O2 •−) can react with the MB molecules to form nontoxic products (Eqs. 8 and 9).

$$CoMoO_4 + h\nu \rightarrow CoMoO_4\,(e^-_{CB} + h^+_{(VB)}) \quad (1)$$

$$(h^+_{VB}) + H_2O \rightarrow H^+ + OH^{\bullet} \quad (2)$$

$$h^+_{VB} + OH^- \rightarrow O\,H^{\bullet} \quad (3)$$

$$e^-_{CB} + O_2 \rightarrow O^{\bullet -} \quad (4)$$

$$H^+ + O_2^{\bullet -} \rightarrow OOH^{\bullet} \quad (5)$$

$$OOH^{\bullet} + OOH^{\bullet} \rightarrow H_2O_2 + O_2 \quad (6)$$

$$H_2O_2 + e^-_{CB} \rightarrow OH^{\bullet} + OH^- \quad (7)$$

$$MB + h\nu \rightarrow MB^{\bullet} \quad (8)$$

$$MB^{\bullet} + (OH^{\bullet}, O_2^{\bullet -}) \rightarrow \text{degradation products} \quad (9)$$

2.5. Dye Degradation Experiment

Using a visible light source, the photocatalytic activity of α- $CoMoO_4$ and β- $CoMoO_4$ and Eu-doped $CoMoO_4$ nanoparticles was evaluated using methylene blue degradation. The magnetic stirrer continuously mixed 50 mg of the nanoparticle with 50 mL of methylene blue (10 mg/L) solution. A transparent double-layered beaker with an intake and outlet nozzle for water circulation was employed for the dye degradation experiment. The height between the vessel bottom and the light source remained constant throughout the trials. The solution was agitated in the dark for about an hour to achieve adsorption equilibrium. The solution was then exposed to light for approximately 4 hours, while 5 mL of the sample solution was obtained at 1-hour intervals. The suspended particles were subsequently removed from the samples by centrifuging them at 3500 rpm for three minutes. The dye's absorbance curve was altered, and the difference was measured using a UV-Visible spectrophotometer. The model dye's absorption peak is located at 664 nm which was confirmed through the UV-Visible analysis. Methylene blue degradation % was determined as follows:

$$Degradation\ efficiency(\%) = \frac{A_0 - A_t}{A_0} \times 100 \quad (10)$$

Where A_0 denotes the starting absorbance and A_t denotes the absorbance at a specific time[31,32]. The as-synthesized catalysts' kinetic characteristics were also investigated utilizing the pseudo-first-order kinetics equation.

$$ln\left(\frac{C_0}{C}\right) = kt \quad (11)$$

where C is the methylene blue sample's absorption intensity at a certain time t (mg L^{-1}), C_0 is the initial dye concentration absorption peak (mg L^{-1}), k is the rate constant (min^{-1}), and t is the light irradiation duration (min) [33,34].

3. Results and discussion

3.1. XRD Analysis

The XRD patterns of the α- $CoMoO_4$, β- $CoMoO_4$ and Eu-doped $CoMoO_4$ nanoparticles are shown in Figure 2a and 2b. The phases of nanoparticle materials with two distinct $CoMoO_4$ crystalline structures were confirmed. The XRD patterns (Fig. 2a, b) reveal that the α- and β- $CoMoO_4$ catalysts have well-defined narrow diffraction maxima for each phase organized throughout a wide range of temperatures. Furthermore, the sharp, high-intensity diffraction peaks show that the as-synthesized catalysts crystallized effectively. In the space group C2/m, the α- $CoMoO_4$ and β- $CoMoO_4$ phases exhibit monoclinic structures. No signals from secondary phases or impurities suggested that the nanoparticles were extremely pure. According to JCPDS cards 00-021-0868 and 00-025-1434, all of the diffraction peaks found for α-$CoMoO_4$ and β-$CoMoO_4$ are easily indexed to the pure phases[26,27].

3.2. Raman analysis

Figures 3 (a) and (b) represent the Raman spectra of $CoMoO_4$, several characteristic bands are observed, each corresponding to specific vibrational modes within the crystal lattice. The most prominent band, typically found around 940 cm^{-1}, is attributed to the symmetric stretching mode of the Mo-O bonds. This mode represents the coordinated motion of oxygen atoms around the molybdenum ions in the lattice structure. The intensity and position of this band can provide information about the strength and symmetry of these bonds, which are crucial for understanding the stability and properties of the material. In addition to the 940 cm^{-1} band, smaller bands are observed in the spectra, spanning a range of wave numbers. These bands typically occur in regions such as 90-240, 280-390, 820, and 880 cm^{-1}. Each of these bands corresponds to specific vibrational modes within the $CoMoO_4$ lattice. For example, the bands at 880 and 820 cm^{-1} are associated with asymmetric stretching modes of oxygen in the O-Mo-O binding environment. These modes involve the stretching of oxygen atoms away from

their equilibrium positions, reflecting the strength and coordination of the bonds in the material. The region between 280 and 390 cm^{-1} encompasses bands associated with bending modes of the O-Mo-O bonds. These bending modes involve the angular motion of oxygen atoms around the molybdenum ions and can provide insights into the flexibility and structural integrity of the lattice. Shifts in the positions of these bands between different phases of $CoMoO_4$ indicate changes in the bond angles and coordination geometry, which are essential for understanding phase transitions and structural transformations. Comparing the Raman spectra of different phases of $CoMoO_4$, such as the α and β phases, reveals subtle differences in the positions, intensities, and shapes of the bands. These differences serve as "fingerprints" for distinguishing between the phases and provide valuable information about their structural properties. For example, bands at 110.6, 129.3, 241.9, and 487.4 cm^{-1} may exhibit differences in intensity or position between the α and β phases, indicating variations in the crystal structure or coordination environment of the molybdenum and cobalt ions [26].

3.3. UV analysis

$CoMoO_4$ nanoparticles are subjected to UV-Vis spectroscopy, distinct absorption peaks are observed, corresponding to electronic transitions within the material. In Figure 4 (a) and (b), the absorption peaks indicate the energy levels at which electrons in the material can absorb photons and transition from the valence band to the conduction band. In the spectra of α and β phases of $CoMoO_4$, absorption peaks at specific wavelengths signify the absorption of light energy by the material, leading to electronic excitations. In the UV-Vis spectra of the $CoMoO_4$ Nano catalyst, distinct absorption peaks were observed, indicating the presence of cobalt molybdate and europium. In the α phase, the absorption peak at 323 nm signifies the transition in the UV region, while the peak at 562 nm and a minor bump at 680 nm suggest additional electronic transitions. Conversely, in the β phase, the absorption peak is broadened and shows higher absorption, indicative of structural changes induced by higher temperature treatment.

The addition of Eu^{3+} to $CoMoO_4$ resulted in a significant shift in the absorption edge towards the visible wavelength region, suggesting modifications in the electronic structure[21].

$$(\alpha h\upsilon)^2 = k(h\upsilon - E_g) \quad (12)$$

The bandgap energy, an essential parameter in semiconductor physics, can be determined from UV-Vis absorbance spectra using Tauc's relation.[35,36] This relationship correlates the absorption coefficient (α) with the photon energy (hυ) and the bandgap energy (Eg). In Figure 5 (a) and (b), By plotting $(\alpha h\upsilon)^2$versus the photon energy (hυ) and extrapolating the linear portion of the curve to the x-axis, the bandgap energy of the material can be estimated. The bandgap energy of α and β phases of $CoMoO_4$, as well as their Eu-doped counterparts, was calculated using Tauc's relation. In the α phase, the bandgap energy for pure $CoMoO_4$ and Eu-doped samples ranged from 2.47 eV to 2.60 eV. Interestingly, the bandgap widened with increasing Eu^{3+} doping up to 5%, after which it began to decrease at 550°C. Contrastingly, the β phase exhibited lower bandgap energies, ranging from 1.98 eV for pure β-CoMoO4 to 2.45 eV for 10% Eu-doped β-CoMoO4. This variation in bandgap energies between the two phases highlights the structural differences and the influence of Eu^{3+} doping on the optical properties of $CoMoO_4$.

3.4. SEM analysis

SEM images of α-$CoMoO_4$, β-$CoMoO_4$, and Eu-doped $CoMoO_4$ composites are depicted in Figures 6 and 7. The images reveal distinctive features of the surfaces, highlighting the morphology and distribution of nanoparticles within the materials. In particular, the $CoMoO_4$/Eu composites exhibit numerous granular-shaped structures, indicating the presence of $CoMoO_4$ nanoparticles dispersed randomly on the surface. The Eu-doped $CoMoO_4$ variant displays an enhanced heterogeneous and porous structure, providing a rough surface with

increased active sites for catalytic reactions. The α- and β-$CoMoO_4$ catalysts exhibit regular morphologies, with the β-polymorphic form displaying spongy-like shapes. These differences in morphology between the α and β forms are readily discernible in the SEM images. Upon annealing at high temperatures, interconnected open-framework structures are formed, contributing to enhanced catalytic properties. The presence of Eu^{3+} nanoparticles within the porous structure introduces additional surface defects, leading to an increase in the number of pores. the materials exhibit a porous structure with interconnected open-frameworks, which suggests the presence of mesopores rather than micropores. These porous characteristics result in a higher surface area, lower density, and improved properties such as light harvesting, electron/ion transport, and mass diffusion, rendering them suitable for various photocatalytic applications.

Moreover, the nanoparticles formed at specific annealing temperatures exhibit unique architectures, such as small dots with bubble wrap configurations, which further enhance catalytic efficiency.

3.5. Evaluation of photo dye degradation

The study investigated the photocatalytic properties of α-$CoMoO_4$, β-$CoMoO_4$, and Eu-doped $CoMoO_4$ at varying concentrations by assessing their ability to degrade methylene blue dye. UV-Visible spectra (Figure 8 and 9) were utilized to observe changes in the absorption intensity of methylene blue solution over different exposure durations to the catalysts. The gradual decrease in the absorption peak intensity of methylene blue at 664 nm indicated a redox reaction induced by the semiconductor nature of the catalyst upon photon interaction.

Percentage degradation of methylene blue by α-$CoMoO_4$, β-$CoMoO_4$, and Eu-doped $CoMoO_4$ nanoparticles at various concentrations was plotted against time in Figure 10. Notably, 10% Eu-doped α-$CoMoO_4$ and β-$CoMoO_4$ exhibited significantly enhanced

photocatalytic activity, achieving degradation rates of up to 96% and 97%, respectively, compared to approximately 92% and 89% for pure α-$CoMoO_4$ and β-$CoMoO_4$. This enhancement underscores the effectiveness of Eu doping in augmenting the photocatalytic activity of $CoMoO_4$, attributed to the reduction in electron-hole pair recombination and the increase in active surface sites facilitated by dopant incorporation.

Furthermore, both α-$CoMoO_4$ and β-$CoMoO_4$ polymorphs demonstrated efficient photocatalytic degradation across different annealing temperatures. The integration of Eu into acidic-based $CoMoO_4$ further enhanced degradation efficiency. Increasing Eu concentration corresponded to improved degradation efficiency, with 10% Eu-doped $CoMoO_4$ achieving complete degradation within 4 hours.

The photo-excitation process occurs when the $CoMoO_4$ photocatalyst absorbs light energy equal to or greater than its band gap energy. Photoinduced holes exhibit stronger oxidizing ability at higher energy valence bands, while photoinduced electrons display enhanced reducing ability at lower energy conduction bands. The positive influence of Eu^{3+} doping can be attributed to the localized energy levels generated upon rare earth metal (Eu^{3+}) incorporation into $CoMoO_4$.

The pseudo-first-order kinetic equation derived from the Langmuir-Hinshelwood model was employed due to the low concentration of methylene blue dye, as illustrated in Figure 11. The linear relationship observed when plotting ln (C_0/C) against time indicates the utilization of first-order kinetics in the photocatalyst's degradation mechanism. Table 1 provided insight into the kinetic properties of the synthesized photocatalysts, including rate constants and R^2 values.

4.Conclusion

The α-$CoMoO_4$, β-$CoMoO_4$, and Eu-doped $CoMoO_4$ nanoparticles prepared from sol-gel synthesis is characterized and proposed for effective photocatalytic dye degradation of methylene blue dye. The two different phases α-$CoMoO_4$ and β-$CoMoO_4$ polymorphs are obtained at different temperatures of about 550°C and 950°C respectively. The as-synthesized nanoparticles exhibit well-defined crystalline structures with porous morphology. Evaluation of photocatalytic degradation of methylene blue highlights superior performance in Eu-doped $CoMoO_4$, particularly at 10% doping. Overall, these nanoparticles show promise for diverse photocatalytic applications, suggesting potential for addressing environmental challenges through efficient pollutant degradation.

Declaration of competing interest

The authors declare that they have no known competing financial interests.

Data availability statement

Data will be available on reasonable request.

References

[1] Raliya R, Avery C, Chakrabarti S, et al. Photocatalytic degradation of methyl orange dye by pristine titanium dioxide, zinc oxide, and graphene oxide nanostructures and their composites under visible light irradiation. Appl Nanosci. 2017;7:253–259.

[2] Wang D, Jia F, Wang H, et al. Simultaneously efficient adsorption and photocatalytic degradation of tetracycline by Fe-based MOFs. J Colloid Interface Sci. 2018;519:273–284.

[3] Zhang Y, Zhou J, Chen X, et al. Coupling of heterogeneous advanced oxidation processes and photocatalysis in efficient degradation of tetracycline hydrochloride by Fe-based MOFs: Synergistic effect and degradation pathway. Chem Eng J

2019;369:745–757.

[4] Yao J, Gong Y, Yang S, et al. $CoMoO_4$ nanoparticles anchored on reduced graphene oxide nanocomposites as anodes for long-life lithium-ion batteries. ACS Appl Mater Interfaces. 2014;6:20414–20422.

[5] Roy K, Sarkar CK, Ghosh CK. Photocatalytic activity of biogenic silver nanoparticles synthesized using potato (Solanum tuberosum) infusion. Spectrochim Acta - Part A Mol Biomol Spectrosc. 2015;146:286–291.

[6] Jana NR, Wang ZL, Pal T. Redox catalytic properties of palladium nanoparticles: surfactant and electron donor-acceptor effects. Langmuir. 2000;16:2457–2463.

[7] Bavykina A, Kolobov N, Khan IS, et al. Metal-Organic Frameworks in Heterogeneous Catalysis: Recent Progress, New Trends, and Future Perspectives. Chem Rev. 2020;120:8468–8535.

[8] Danish Khan M, Abdulateif H, Ismail IM, et al. Bioelectricity generation and bioremediation of an azo-dye in a microbial fuel cell coupled activated sludge process. PLoS One. 2015;10.

[9] Sahu K, Dhonde M, Murty VVS. Preparation of copper/TiO_2/ graphene oxide ternary nanocomposites and their structural, surface morphology, and optical properties. J Mater Sci Mater Electron. 2021;32:15971–15980.

[10] Santhana V, Thangaraju D, Tanaka A, et al. Development of Hybrid TiO_2/Paint Sludge Extracted Microbe Composite for Enhanced Photocatalytic Dye Degradation. J Inorg Organomet Polym Mater. 2020;30:2805–2813.

[11] Karuppasamy P, Ramzan Nilofar Nisha N, Pugazhendhi A, et al. An investigation of transition metal doped TiO_2 photocatalysts for the enhanced photocatalytic

decoloration of methylene blue dye under visible light irradiation. J Environ Chem Eng. 2021;9:105254.

[12] Chong MN, Jin B, Chow CWK, et al. Recent developments in photocatalytic water treatment technology: A review. Water Res. 2010;44:2997–3027.

[13] Sahu K, Dhonde M, Murty VVS. Microwave-assisted hydrothermal synthesis of Cu-doped TiO_2 nanoparticles for efficient dye-sensitized solar cell with improved open-circuit voltage. Int J Energy Res. 2021;45:5423–5432.

[14] Dhonde M, Dhonde KS, Murty VVS. Novel sol–gel synthesis of Al/N co-doped TiO_2 nanoparticles and their structural, optical and photocatalytic properties. J Mater Sci Mater Electron. 2018;29:18465–18475.

[15] Vinayagam R, Pai S, Varadavenkatesan T, et al. Characterization and photocatalytic activity of ZnO nanoflowers synthesized using Bridelia retusa leaf extract. Appl Nanosci. 2023;13:493–502.

[16] Vinayagam R, Pai S, Murugesan G, et al. Synthesis of photocatalytic zinc oxide nanoflowers using Peltophorum pterocarpum pod extract and their characterization. Appl Nanosci. 2023;13:847–857.

[17] Liu F, Leung YH, Djurišić AB, et al. Native defects in zno: Effect on dye adsorption and photocatalytic degradation. J Phys Chem C. 2013;117:12218–12228.

[18] Singh P, Sharma K, Hasija V, et al. Systematic review on applicability of magnetic iron oxides–integrated photocatalysts for degradation of organic pollutants in water. Mater Today Chem. 2019;14:100186.

[19] Zhao Y, Xu Z, Fu H, et al. Swallow-Nest Architectures with Cobalt Molybdate Particulates Fixed Constructed Carbon Nanotube Supports for Stable Sodium-Ion

Battery Anode. J Electrochem Soc. 2020;167:080528.

[20] Nasri R, Larbi T, Khemir H, et al. Photocatalytic efficiency of $Na_4Co(MoO_4)_3$ for the degradation of industrial azo dye under solar irradiation. Inorg Chem Commun. 2020;119.

[21] Seevakan K, Manikandan A, Devendran P, et al. Electrochemical and magneto-optical properties of cobalt molybdate nano-catalyst as high-performance supercapacitor. Ceram Int. 2018;44:17735–17742.

[22] Ahmad I. Inexpensive and quick photocatalytic activity of rare earth (Er, Yb) co-doped ZnO nanoparticles for degradation of methyl orange dye. Sep Purif Technol. 2019;227:115726.

[23] Faraz M, Naqvi FK, Shakir M, et al. Synthesis of samarium-doped zinc oxide nanoparticles with improved photocatalytic performance and recyclability under visible light irradiation. New J Chem. 2018;42:2295–2305.

[24] Samuel P, Thangaraju D, Babu SM. Effect of dysprosium active ions on spectral properties of KGW single crystals. J Alloys Compd. 2011;509:177–180.

[25] Balaji D, Durairajan A, D.thangaraju, et al. Investigation of structural and luminescent properties of Pr^{3+} activated $CsGd(WO_4)_2$ by sol-gel synthesis. Mater Sci Eng B. 2013;178:762–767.

[26] Rodriguez M, Stolzemburg MCP, Bruziquesi CGO, et al. Electrocatalytic performance of different cobalt molybdate structures for water oxidation in alkaline media. CrystEngComm. 2018;20:5592–5601.

[27] Costa RKS, Teles SC, de Sousa Filho PC, et al. Influence of europium doping on the structural phase-transition temperature of β− and α−$CoMoO_4$ polymorphs. Mater Res

Bull. 2019;118.

[28] Vinayagam R, Hebbar A, Senthil Kumar P, et al. Green synthesized cobalt oxide nanoparticles with photocatalytic activity towards dye removal. Environ Res. 2023;216:114766.

[29] Amreetha S, Dhanuskodi S, Nithya A, et al. Three way electron transfer of a C-N-S tri doped two-phase junction of TiO_2 nanoparticles for efficient visible light photocatalytic dye degradation. RSC Adv. 2016;6:7854–7863.

[30] Ansari SA, Khan MM, Ansari MO, et al. Visible light-driven photocatalytic and photoelectrochemical studies of Ag-SnO_2 nanocomposites synthesized using an electrochemically active biofilm. RSC Adv. 2014;4:26013–26021.

[31] Thilagavathi T, Venugopal D, Marnadu R, et al. WO_3/$CoWO_4$ nanocomposite synthesis using a facile co-precipitation method for enhanced photocatalytic applications. J Phys Chem Solids. 2021;154:110066.

[32] Shanmugam P, Dheivasigamani T, Moorthy Babu S, et al. A facile sol–gel synthesis and characterization of europium (Eu) doped β-$Bi_2Mo_2O_9$ nanoparticles with remarkably enhanced photocatalytic activity for waste-water treatments. Inorg Chem Commun. 2022;146:110163.

[33] Prakash N, Thangaraju D, Karthikeyan R, et al. UV-visible and near-infrared active $NaGdF_4$:Yb:Er/Ag/TiO_2 nanocomposite for enhanced photocatalytic applications. RSC Adv. 2016;6:80655–80665.

[34] Prakash N, Karthikeyan R, Thangaraju D, et al. Effect of Erbium on the Photocatalytic Activity of TiO_2/Ag Nanocomposites under Visible Light Irradiation. ChemPhysChem. 2015;16:3084–3092.

[35] Shunmughananthan B, Dheivasigamani T, Sthevan Kovil Pitchai J, et al. Performance comparison of distinct bismuth molybdate single phases for asymmetric supercapacitor applications. Dalt Trans. 2022;51:15579–15592.

[36] Seerangan Selvam G, Sthevan Kovil Pitchai J, Ammasai K, et al. Performance analysis of three distinct $Ni_xV_2O_y$ single-phase nano self-assemblies for asymmetric supercapacitor fabrication and effective detection of low-concentration hazardous herbicide. Dalt Trans. 2023;52:14491–14509.

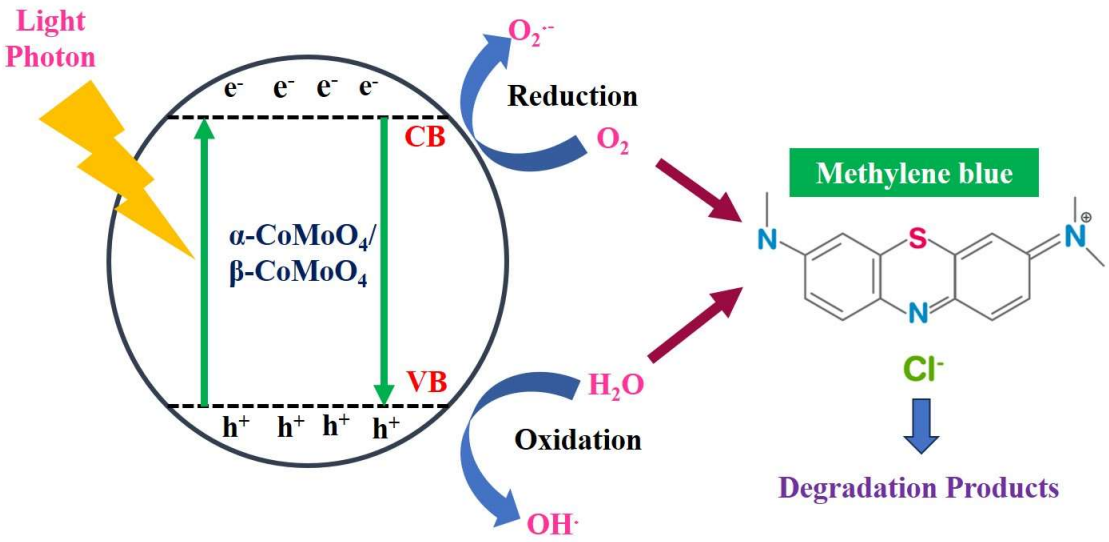

Figure 1: Schematic illustration showing the possible photocatalytic mechanism for the photodegradation of MB dye

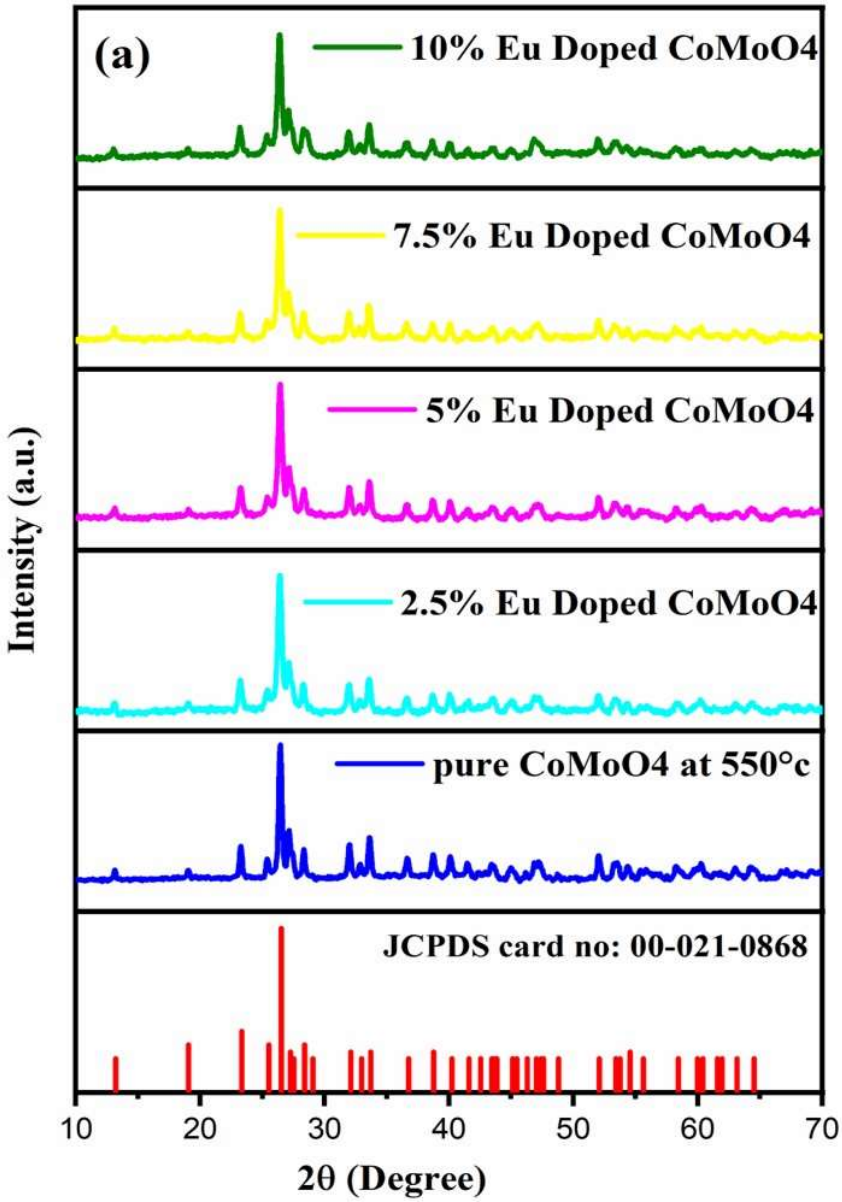

Figure 2a: Comparative XRD patterns of α-$CoMoO_4$ (550°C), 2.5%, 5%, 7.5% and 10 % Eu: α-$CoMoO_4$

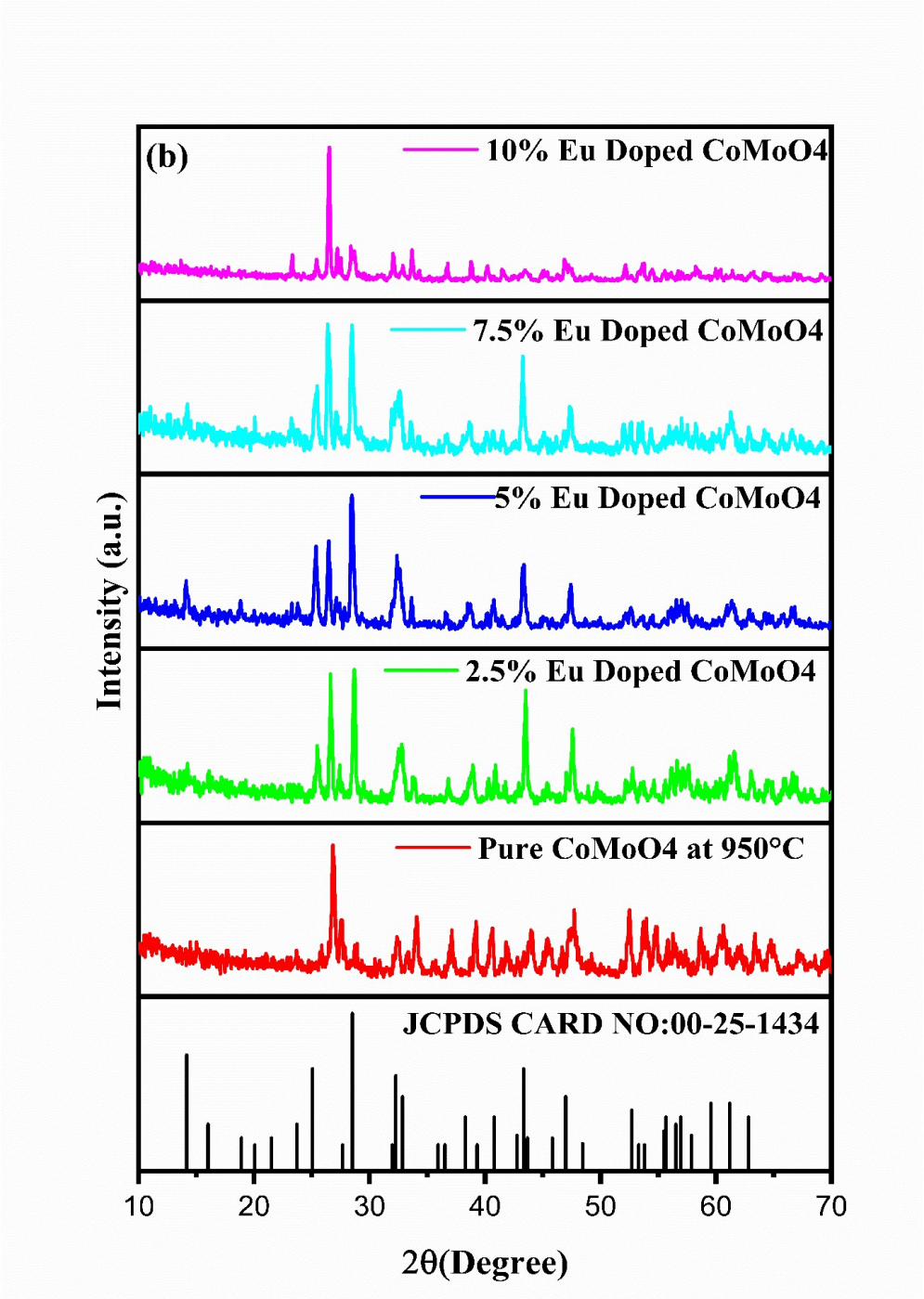

Figure 2b: Comparative XRD patterns of β-$CoMoO_4$ (950°C) and 2.5%, 5%, 7.5% and 10 % Eu: β-$CoMoO_4$

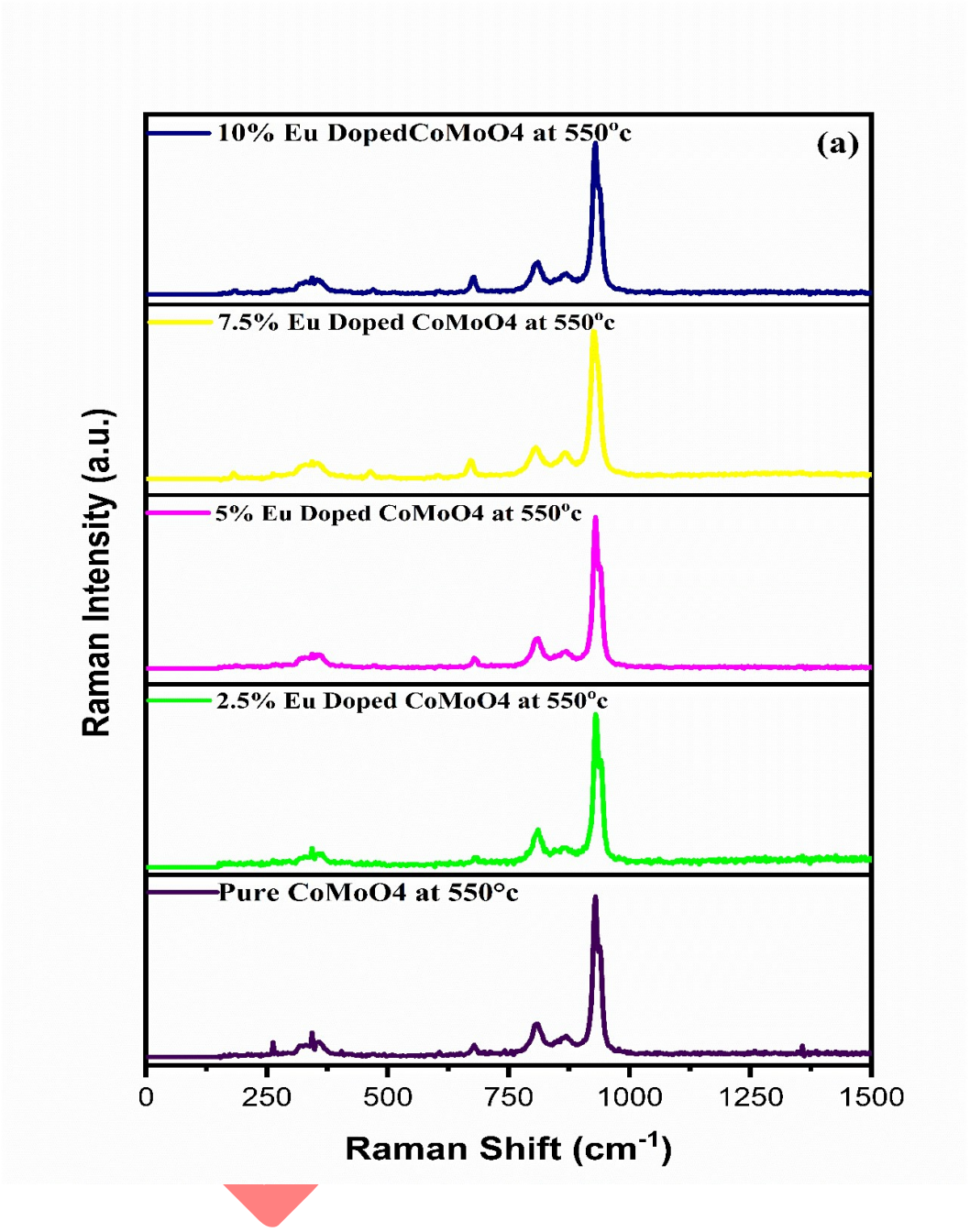

Figure 3a: Raman Spectra of β-$CoMoO_4$ (550°C) and 2.5%, 5%, 7.5% and 10 % Eu: β-$CoMoO_4$

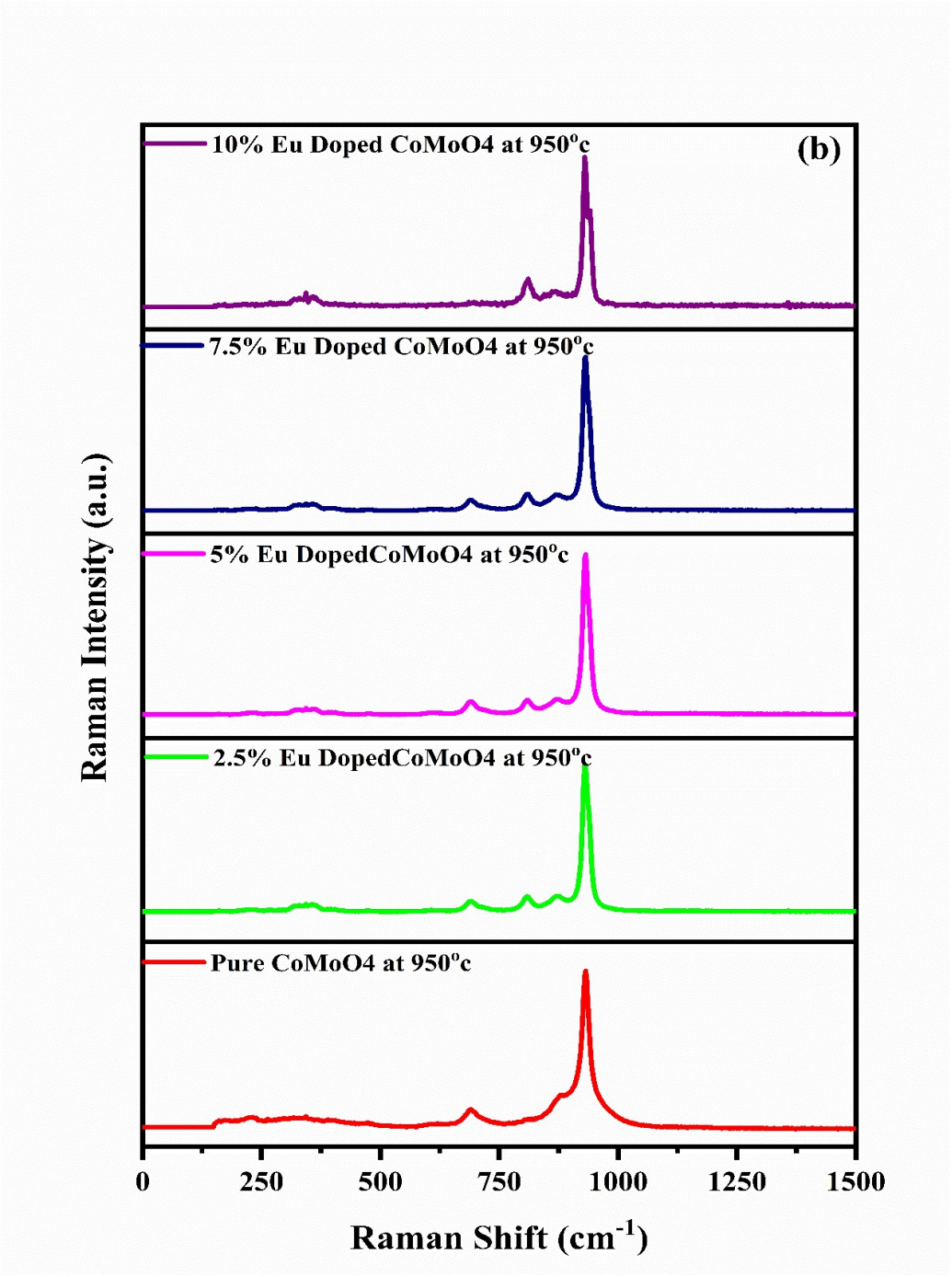

Figure 3b: Raman Spectra of β-$CoMoO_4$ (950°C) and 2.5%, 5%, 7.5% and 10 % Eu: β-$CoMoO_4$

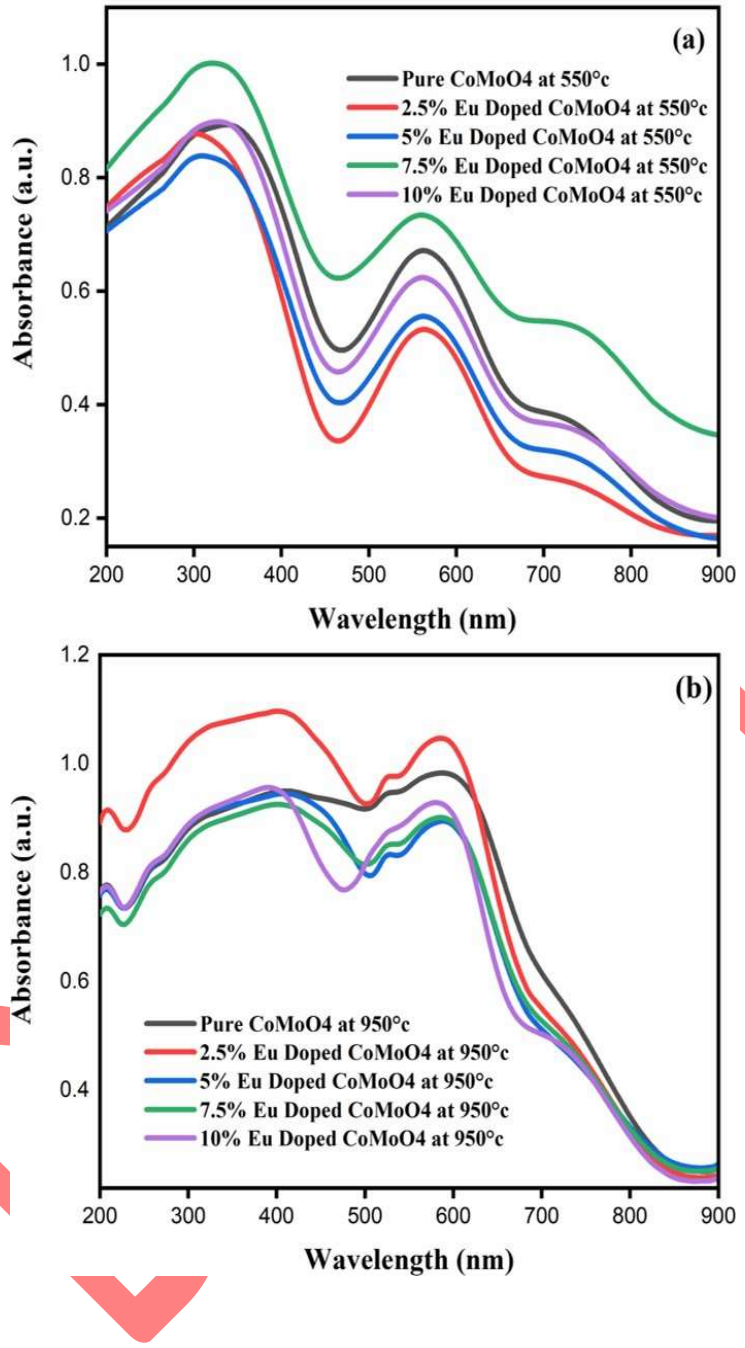

Figure 4: UV absorbance spectra of (a) α-$CoMoO_4$ (550°C) 2.5%, 5%, 7.5% and 10 %Eu: α-$CoMoO_4$, and (b) β-$CoMoO_4$ (950°C) and 2.5%, 5%, 7.5% and 10 % Eu: β-$CoMoO_4$

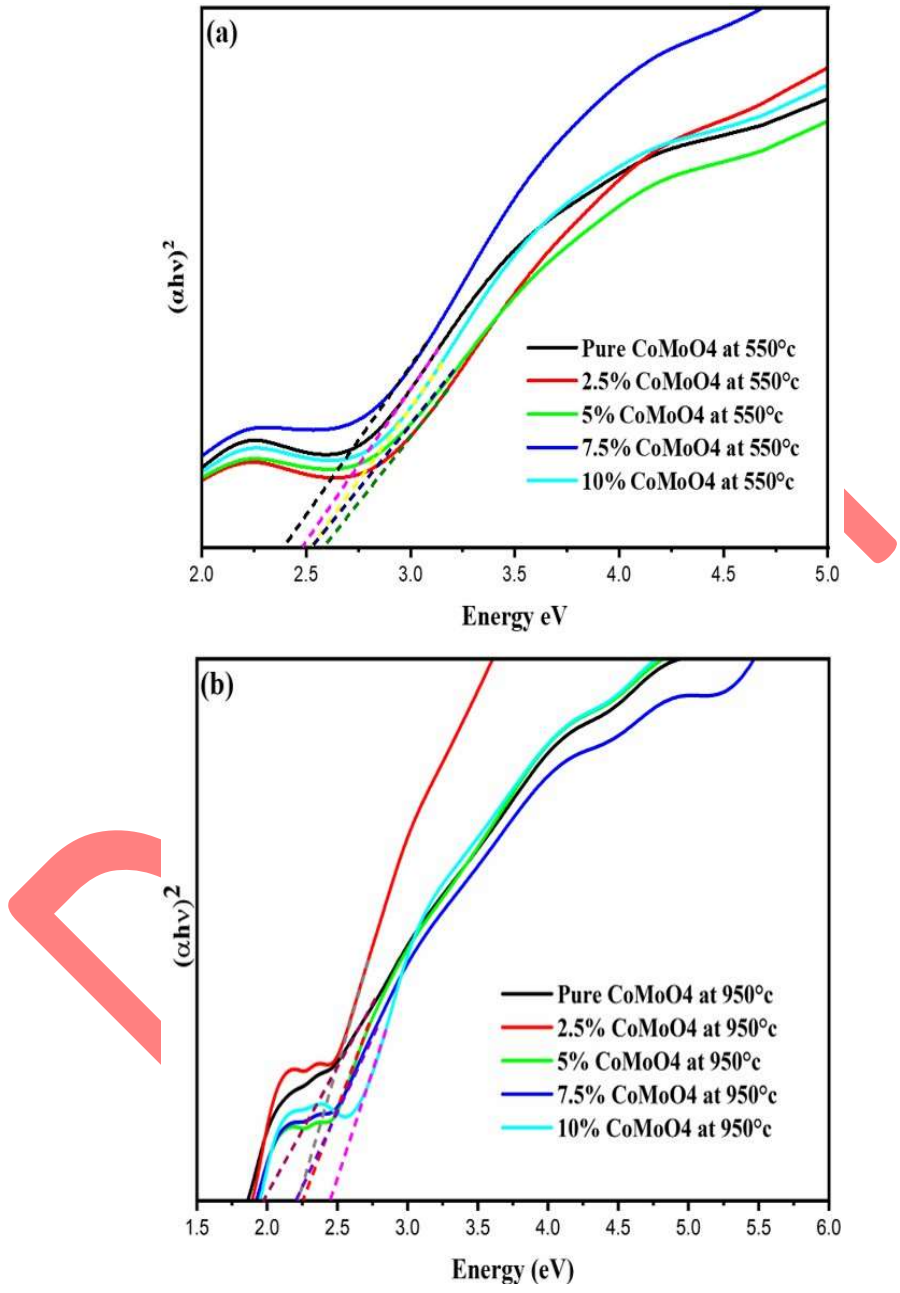

Figure 5: Tauc plot for the band gap evaluation of (a) α-$CoMoO_4$ (550°C), 2.5%, 5%, 7.5% and 10 % Eu: α-$CoMoO_4$, and (b) β-$CoMoO_4$ (950°C)and 2.5%, 5%, 7.5% and 10 % Eu: β-$CoMoO_4$

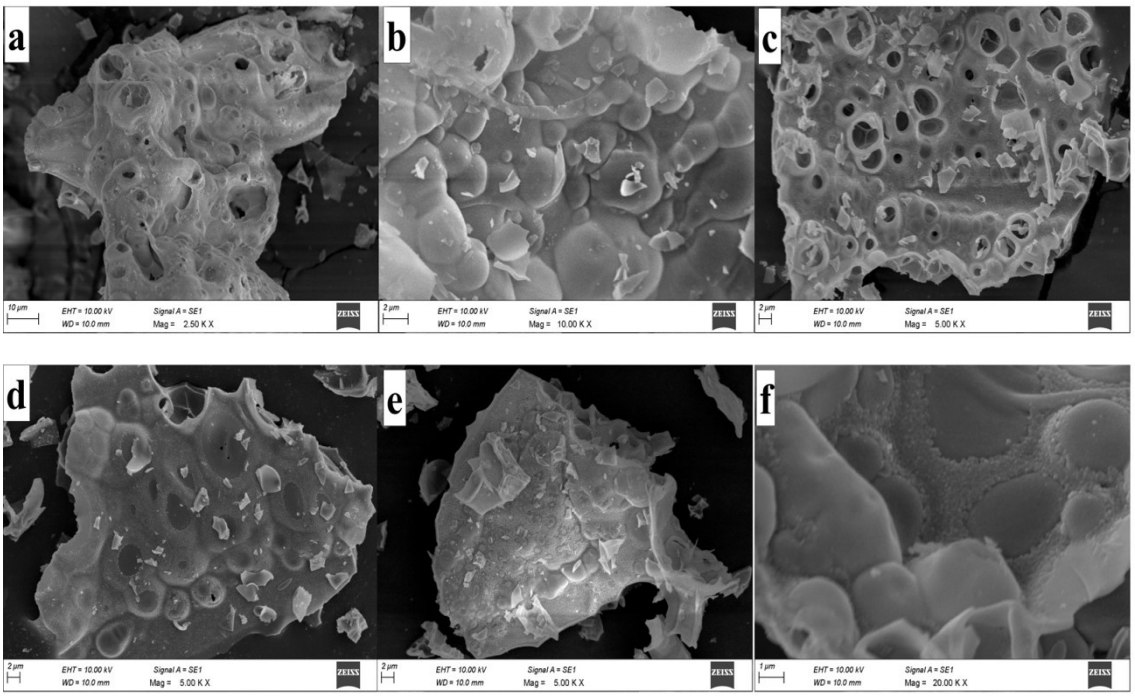

Figure 6: SEM images of α-$CoMoO_4$ (550°C) (a-f). (a)Pure α-$CoMoO_4$, (b)2.5%, (c) 5%, (d) 7.5%, (e) and (f) 10% of α-$CoMoO_4$

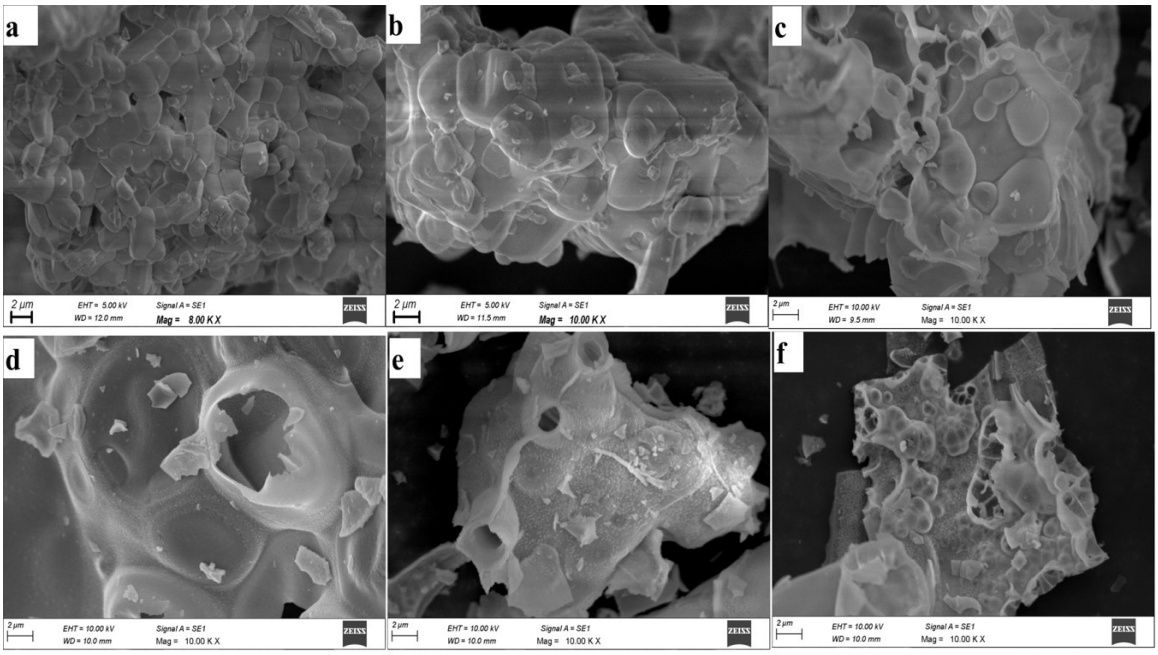

Figure 7: SEM images of β-$CoMoO_4$ (950°C) (a-f). (a) Pure β-$CoMoO_4$, (b) 2.5%, (c) 5%, (d) 7.5%, (e) and (f) 10 %Eu: β-$CoMoO_4$

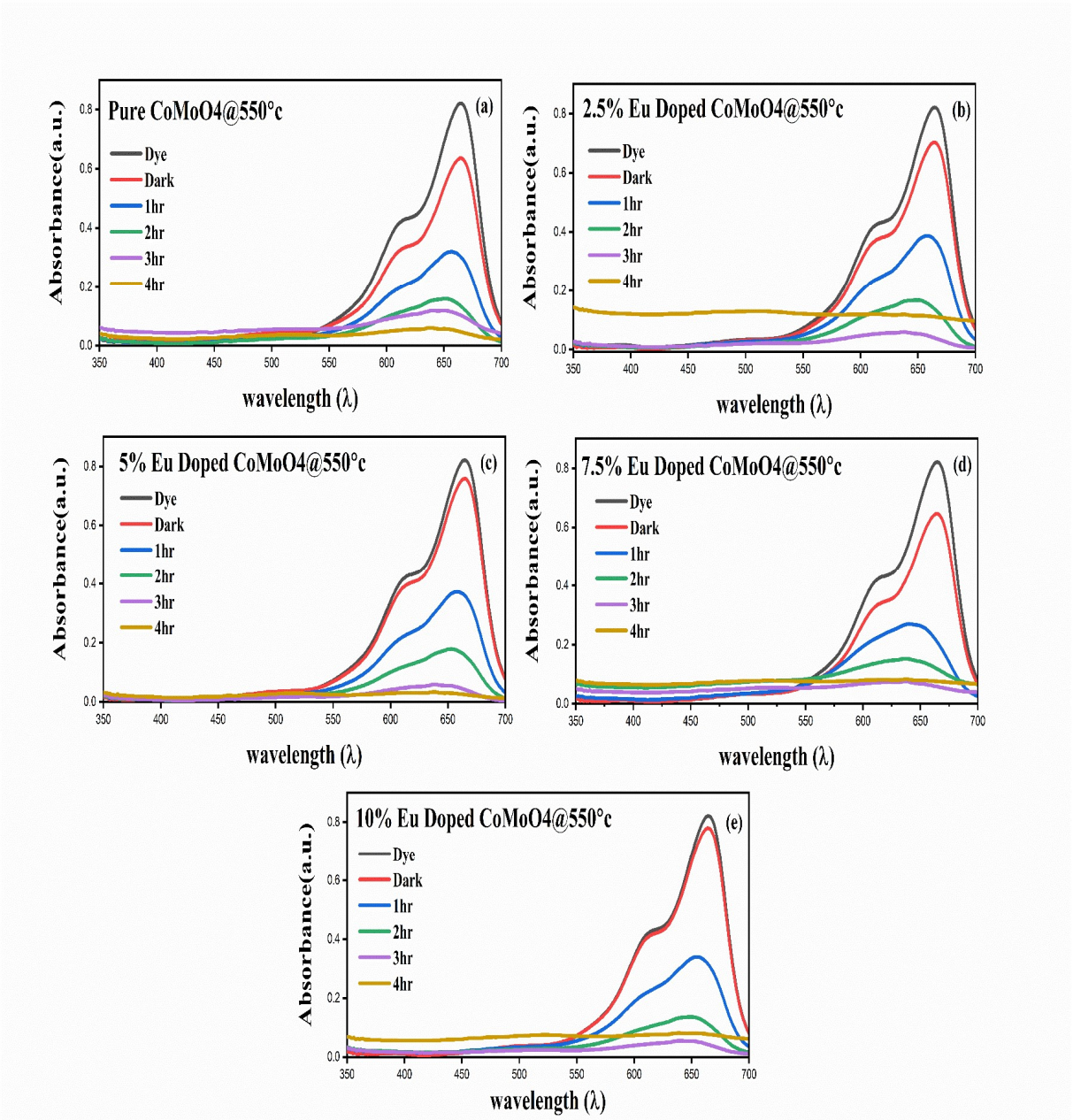

Figure 8: Photocatalytic degradation of methylene blue using α-$CoMoO_4$ (550°C), 2.5%, 5%, 7.5% and 10 % Eu: α- $CoMoO_4$

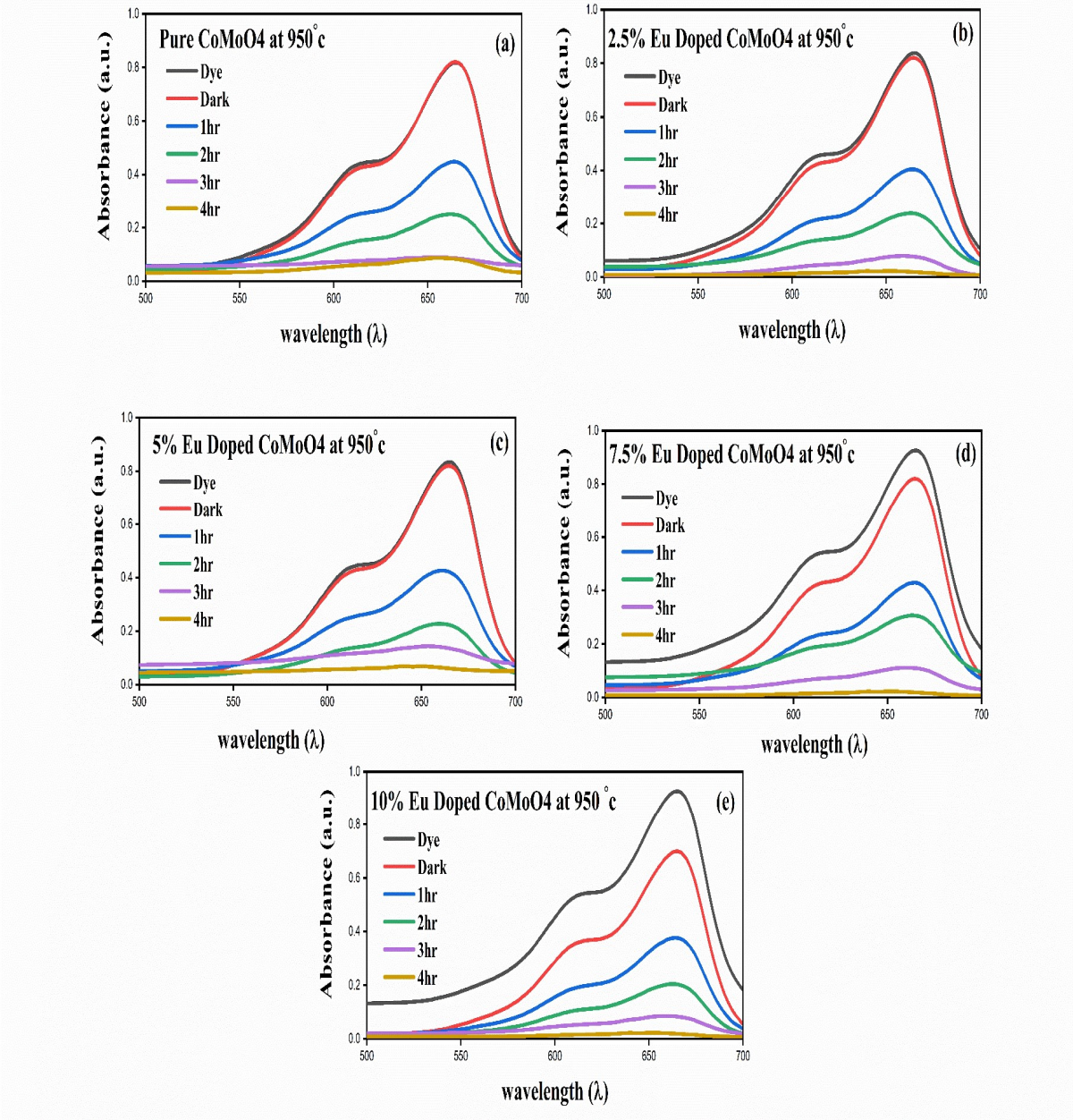

Figure 9: Photocatalytic degradation of methylene blue using β-$CoMoO_4$ (950°C), 2.5%, 5%, 7.5% and 10 % Eu: β-$CoMoO_4$

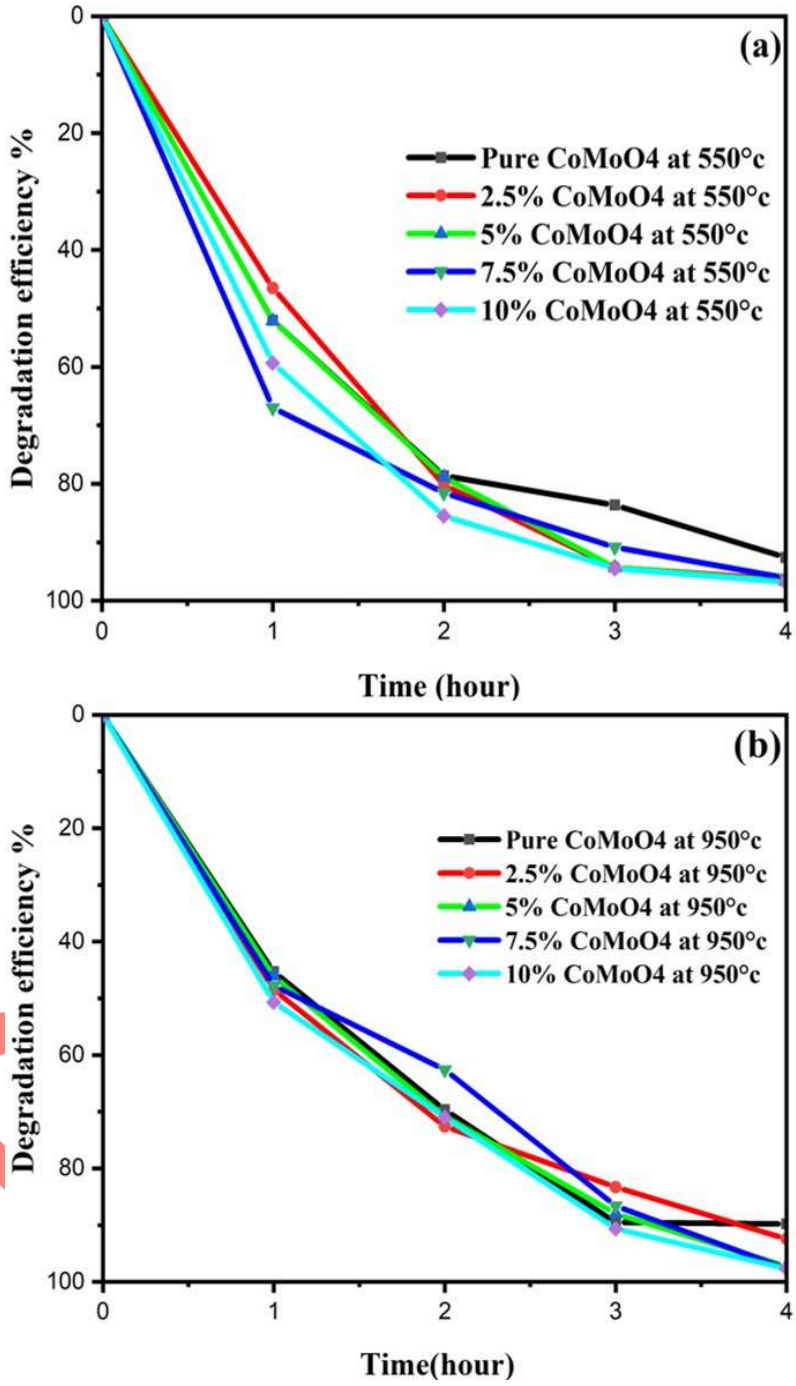

Figure 10: Degradation percentage of methylene blue dye by (a) α-$CoMoO_4$ (550°C), 2.5%, 5%, 7.5% and 10 % Eu: α-$CoMoO_4$ and (b) β-$CoMoO_4$ (950°C), 2.5%, 5%, 7.5% and 10 % Eu: β-$CoMoO_4$

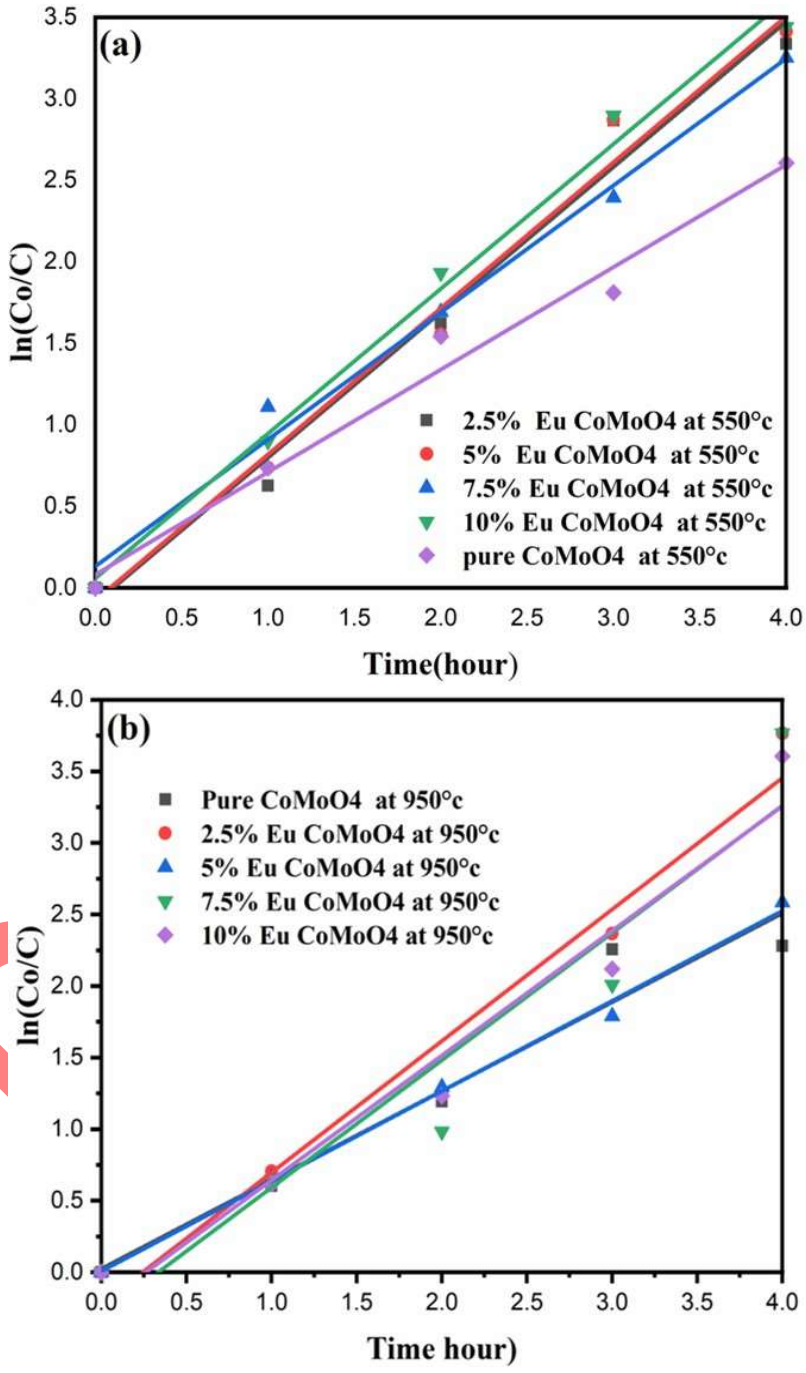

Figure 11: The kinetic plot for the degradation of methylene blue of α-$CoMoO_4$ and β-$CoMoO_4$

Kinetic Model	Parameter	$CoMoO_4$	2.5% Eu $CoMoO_4$	5% Eu $CoMoO_4$	7.5% Eu $CoMoO_4$	10% Eu $CoMoO_4$
First order (550°C)	Rate Constant (k) ($hour^{-1}$)	0.6286	0.8913	0.8956	0.7787	0.88785
	R^2(COD)	0.98177	0.98231	0.98598	0.98979	0.9906
First order (950°C)	Rate Constant (k) ($hour^{-1}$)	0.62121	0.91922	0.62942	0.88931	0.87119
	R^2(COD)	0.95166	0.96375	0.99598	0.91598	0.95891

Table 1: The kinetic parameters of as-synthesized α- $CoMoO_4$ and β- $CoMoO_4$ photocatalysts